Full length article

Advancing frequency locking: Modified FPGA-Guided direct modulation spectroscopy for laser stabilization

Prosenjit Majumder [a,b,*], Hemant Yadav [b], Rakesh Tirupathi [b,c], Kamalkant [b], Shruti Jain [b], Poonam Yadav [b], Arnab Ghosh [b], Apoorav Singh Deo [b], Deepshikha Singh [b]

[a] *Tampere University, Photonics Laboratory, Physics Unit, Tampere, FI-33720, Finland*
[b] *Department of Physics, Indian Institute of Technology, Delhi, Hauz Khas, Delhi, 110016, New Delhi, India*
[c] *Department of Electrical and Computer Engineering, National University of Singapore, 117583, Singapore*

ARTICLE INFO

ABSTRACT

In this paper, we propose a cost-effective laser frequency locking scheme based on frequency modulation spectroscopy (FMS) for precision measurements and experiments in various fields. We demonstrate that by digitally modulating the detected signal frequency using a Field-Programmable-Gate-Array (FPGA) driven by a home-built lock-in and a proportional–integral–derivative (PID) control system, our system achieves higher precision, user-friendliness, and versatility. Our system generates a 20 V peak-to-peak amplified voltage to a piezo transducer (PZT), which enables a mode-hop free laser scan of approximately 2 $\pm$0.2 GHz. We directly modulate the detected saturation absorption signal with a sinusoidal waveform, then demodulate it to obtain multiple zero crossing locking points on the D2 transition of Cs at 852.35 nm. We optimized the system for three commonly used atomic transitions and found that researchers can select any of the zero crossing peaks for frequency stabilization depending on their experimental requirements, we locked the laser at the crossover transition. We measured the long-time frequency fluctuation and power spectral density and found that the frequency fluctuation of the laser is much less than the natural line width of the D2 transition of Cs. Our results demonstrate that our laser frequency locking scheme is effective and practical for precision measurements and experiments in various fields.

1. Introduction

Frequency-stable laser sources such as Bose–Einstein condensation, optical atomic clocks, quantum gravimeters, and ultra-cold molecular physics are crucial for laser cooling and trapping experiments. To achieve this, kHz-level frequency stabilization technology is essential for fundamental science [1], quantum navigation [2], and highly sensitive ground and space-based quantum sensors [3,4]. However, the complete system requires dedicated physical components and complex control hardware for stabilizing the laser frequency. The conventional system is comparatively large, necessitates various electronic components, and demands considerable space. Recent experiments in atomic physics demand compact sub-systems that can operate at significantly high speeds and can be controlled digitally.

The Field-programmable Gate Array (FPGA)-based locking system reduces the subsystem size compared to the traditional system. It provides high temporal resolution and high-speed data transfer on control outputs and acquisition inputs. Moreover, FPGA-based electronics are highly re-configurable and offer the possibility of a conditional control

spectrum digitally. These properties can be used as ideal platforms to realize locking circuits [5,6]. The FPGA-based system can also be used for optomechanical systems [7], cold atom experiments [8,9], experiments with Diamond Nitrogen-Vacancy [10], and the operation of Ion traps [11]. Recently, the high availability of FPGA chips made them cost-effective, and they have been used at cryogenic temperatures, making them attractive for the management of several quantum information systems [12].

Recently, the Red Pitaya STEMlab-based FPGA has been accepted by the scientific organization for several real-life applications, including locking-in amplification, laser frequency, and intensity stabilization [6,13]. But no one has systematically characterized and studied the direct frequency modulation of the saturation absorption spectroscopic (SAS) spectrum with improved scan range. In addition, one can generate random waveforms/functions, including generators using the Red Pitaya. Also, the Red Pitaya offers satisfactory timing resolution but is restricted in control functionality and input or output channels. FPGA-based systems are very beneficial for high-time resolution and
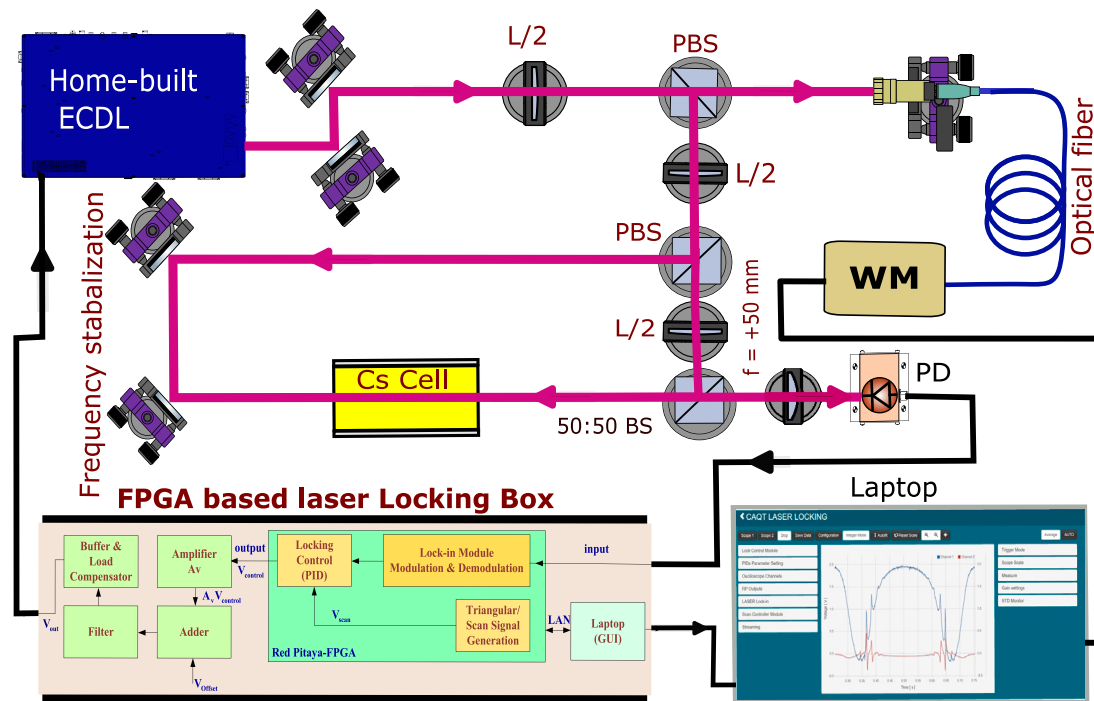
Fig. 1. The experimental setup consists of an External-Cavity Diode Laser (ECDL) producing the required laser beam. The beam passes through a half wave-plate (L/2) and a polarizing beam splitter (PBS). One arm of the beam goes into a wavelength meter (WM), while the other arm overlaps with the pump beam and the probe beam inside the vapor cell. The probe beam is focused through the f = +50 mm lens into a photo-diode (PD). The photodetector signal is directed to the FPGA-based locking box, where it undergoes simultaneous modulation and demodulation processes. This setup allows for the generation of a scan signal, which is precisely controlled by the PID unit. The signal is subsequently amplified, subjected to offset addition, filtered, and finally passed through a buffer and load compensator to produce the feedback signal. This feedback signal is then recorded using a graphical user interface (GUI) via a digital interface, typically on a laptop. The feedback signal is sent back to the laser to stabilize its frequency. The digital feedback control system is also shown in the schematic diagram.

considerable bandwidth applications, but due to limited specialized knowledge of the programming community, having some obstacles.

This paper introduces a compact laser frequency stabilization system and an FPGA-based laser locking amplifier circuit that can fine-tune laser frequency without touching the grating. The system is based on the inexpensive Xilinx Zynq-7010 Red Pitaya STEMlab board, which offers a timing resolution of 8 ns and a bandwidth of ~125 MHz for 14 digital output channels. We can take advantage of its open-source logic design capabilities and tailor the code to suit our specific application. To achieve our locking objectives, we have developed a customized code and graphical user interface (GUI) that integrates seamlessly into our design. The code customization is implemented on an FPGA to ensure efficient locking operations. We can control every parameter of the laser through the modified home-built GUI, including the laser ramp voltage, locking, and digitally monitoring the detected absorption spectrum. We demonstrate the routine use of these modules in controlling lasers and locking the laser using the frequency modulation spectroscopy (FMS) technique. The paper is organized into four parts: (i) a detailed description of the optical setup, (ii) details of the homebuilt electronics used to drive and lock the laser, (iii) optimization of experimental FM spectroscopy, and (iv) evaluation of the long-time frequency fluctuation and power spectral density (PSD) spectrum before and after locking to determine the qualitative difference.

2. Optical setup design

Our frequency reference study is based on FM spectroscopy, where we digitally modulate the SAS spectrum by changing the frequency and amplitude of detected signals. Our optical setup includes a compact home-built External-cavity diode laser (ECDL) in Littrow configuration with a cavity length of 15 mm and a free spectral range of 10 GHz. After optimizing the beam's position and size, we split it into two parts. One part goes to a wavelength meter (WM) to continuously monitor the

beam's wavelength, while the other part is used in the spectroscopic experiment. The beam was divided into two parts using a half-wave plate and a polarizing beam splitter. One part served as the probe beam, and the other as the pump beam. Both beams were made to overlap inside the vapor cell, where they interacted with atoms in a non-linear fashion, resulting in the generation of the SAS spectrum of the D2-line of Cesium (Cs) at 852.35 nm. The spectrum was detected by focusing the probe beam using an f = +50 mm lens into a home-built photo-diode (PD) with a responsivity of approximately 0.55 A/W and a 35 MHz bandwidth. The detected SAS spectrum was sent to the input of the compact locking system, which could be monitored using the interface shown in Fig. 1. The locking device consists of two main components: an FPGA-based stand-alone system and an electronic sub-system. The circuit generates an amplified ramp signal, which is sent to the input Piezo as a laser ramp. The Red Pitaya is used to modulate the SAS spectrum by beating it with a sinusoidal signal of specific frequency and amplitude. This results in an FM spectrum with multiple zero crossings. Once a lock point is selected at a specific atomic transition, the proportional–integral–derivative (PID) controller is activated to compensate for voltage fluctuations in the laser spectrum. The laser Piezo then forms a closed loop, allowing the system to follow the loop for long-term laser frequency stability continuously.

To achieve stability, reduce bulkiness, and increase compactness, a laser-controlling box has been designed using 3D printing technology. This box has been designed to allow for the components to be mounted on the walls of the box, and the power supply has been integrated into the box itself. This resulted in a compact and easy-to-use plug-and-play system, as depicted in Fig. 2(a). The customized GUI based on previous work [6,13], is capable of generating ramp signals, modulation spectra, demodulation of spectroscopy spectra, and frequency locking (locked/unlocked). Furthermore, the system features an RGB-LED that indicates the device status (idle, running, error). The back panel of the box provides access to the Red Pitaya's interface, which
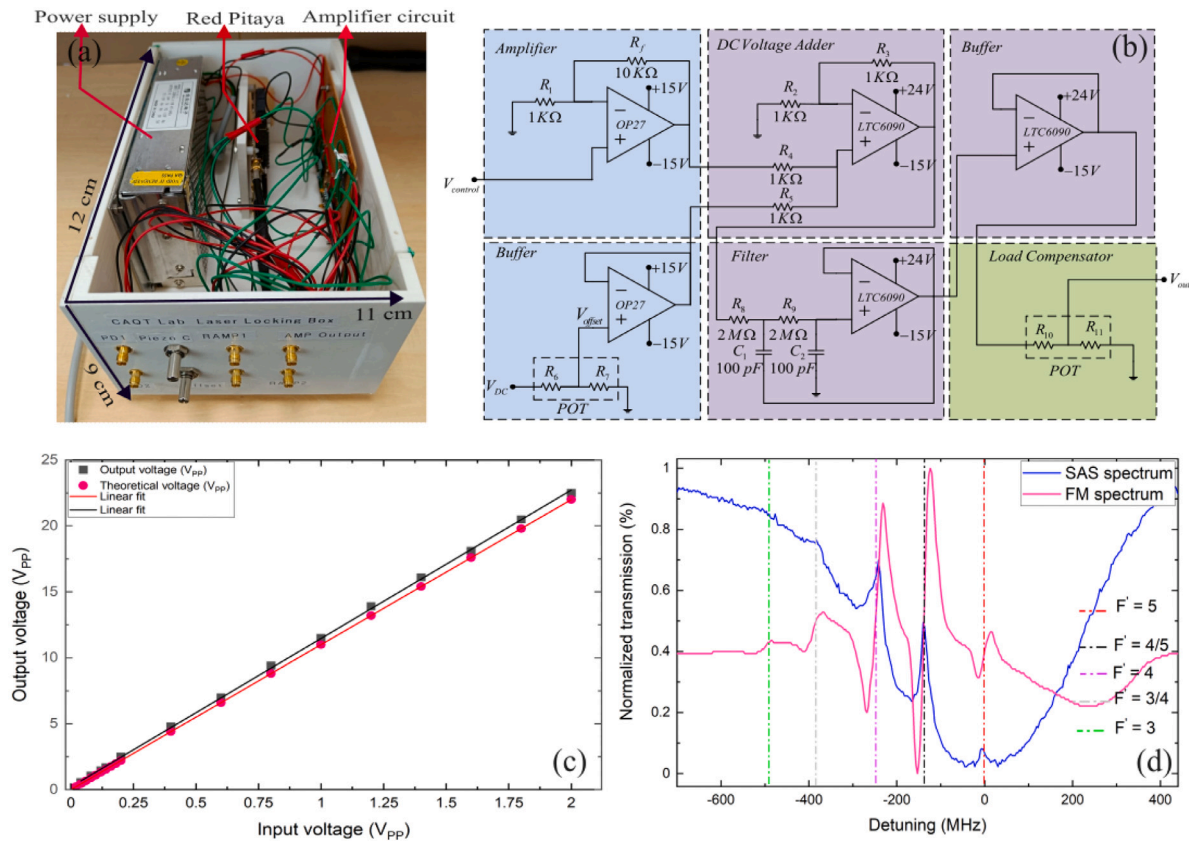
Fig. 2. The system is presented in (a) with the primary electronic components, and the characterized data and FM signals are displayed. It showcases the hardware integration of the FPGA-based laser locking box, which measures 12 cm × 11 cm × 9 cm. The innovative electronic design of the laser locking circuit is depicted in (b) and labeled accordingly. The electronic circuit's characteristic plots are displayed in (c), with the black data point representing the voltage output with the input voltage, and the red data point representing the theoretical prediction of experimental data. Finally, in (d), the saturation absorption and FM spectroscopy signals' blue and purple lines are illustrated, demonstrating all visible hyper-fine transitions.
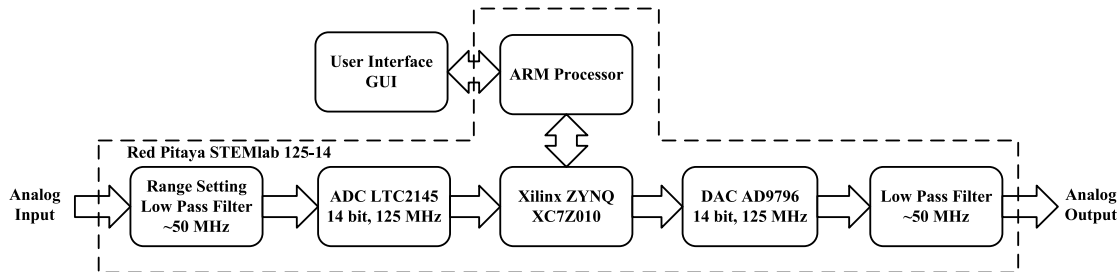

Fig. 3. Block diagram of working principle of a Red Pitaya.

includes connectors for the power supply (micro-USB), USB type A, and Ethernet for the digital interface/laptop, as shown in Fig. 1.

3. Lock-box electronics design

The generated ramp signal is directly applied to the laser's PZT, and the laser beam passes through a Cs vapor cell at a wavelength of 852.35 nm. A photo-diode (FDS 100, with 35 MHz bandwidth where the load resistance (R_L) is 50 Ω) detects the beam's intensity and produces a signal in the millivolt range proportional to the beam's intensity. This signal requires processing to reduce noise and emphasize the essential locking parameters. To address this, an innovative locking box circuit has been developed using FPGA technology and discrete components, as shown in Fig. 2(a) and (b). The circuit's functionality has been confirmed using the test setup demonstrated in Fig. 2(c), which illustrates the correlation between the input voltage and the output voltage of the circuit depicted in Fig. 2(b). Within the locking

system, the primary signal is a triangular scan signal, generated by the Red Pitaya, featuring programmable amplitude and frequency.

The locking box is equipped with a Red Pitaya programmed with Verilog coding to offer functions like a triangular/scan signal generator, lock-in amplifier, locking controller, and proportional–integral–derivative controller (PID) [14]. The Red Pitaya produces an output voltage within the ±1 Volt range, which is processed through a series of discrete component-built circuits consisting of a voltage amplifier, DC voltage adder, filter, buffer, and load compensator. After processing, a 20 V (peak-to-peak) signal is generated and fed to the piezo-actuator for scanning while the PID is activated to regulate the actuation displacement. The signal $V_{control}$ represents the signal generated by the Redpitaya, while the V_{out} signal corresponds to the amplified and filtered signal. The key innovation lies in the circuit design, which amplifies the signal and introduces an offset to shift the signal. For filtering purposes, a Sallen-Key low pass filter topology has been employed, and the filter parameters are determined using Eq. (4).

3.1. Red pitaya

The laser locking box is built around the Red Pitaya system-on-chip (SOC) based on a dual-core ARM Cortex-A9 processor. The system's block diagram is shown in Fig. 3, with two 14-bit analog-to-digital converters (ADCs) and two 14-bit digital-to-analog converters (DACs), the Red Pitaya can perform high-speed data acquisition. The system's data conversion rate is 125 MHz, which is suitable for laser locking applications. Low-pass FIR and IIR filters are available on the system to remove unwanted noise digitally. The FPGA is programmed using Verilog coding [14] to perform various functions, such as generating triangular/scan signals, lock-in amplification, and PID control. The Red Pitaya offers a web-based GUI to interact with the lockbox circuit and adjust real-time parameters, such as the lock-in time constant and the PID gains.

3.2. Triangular signal generator

The primary function of the triangular/scan signal generator is to move the piezo mirror within the voltage range of 0 to 20 V. This is achieved by producing a triangular waveform that linearly displaces the mirror position as it increases and decreases. This enables precise determination of the lock-in position. The Verilog code is used to implement the signal logic, which is then programmed into the FPGA to control the piezo actuator. However, the output voltage range of the Red Pitaya DAC is limited to ± 1 Volt, and to achieve the desired voltage range of 0 to 20 V, an external circuit is employed to amplify the triangular signal. This range corresponds to a mode hop-free laser scan in the frequency domain of approximately 2 ± 0.2 GHz. The limitation on the output voltage range is due to the availability of a suitable power supply and the semiconductor chip.

3.3. Lock-in amplifier

The signal selected for locking is processed by the lock-in amplifier, which modulates it with a carrier signal from a local oscillator. The lock-in amplifier is capable of performing standard harmonic lock-in and square wave lock-in, as reported in [14]. In this experiment, the optimized carrier frequency for the standard lock-in is 3.82 ± 0.04 kHz, while the square wave lock-in can operate up to 31 MHz. The modulated signal is subsequently routed through a low-pass filter designed to eliminate any undesirable noise. For this specific experiment, an optimal cut-off frequency of 307.1 kHz has been determined. A comprehensive investigation of the modulation process has been conducted and is presented in Fig. 4.

3.4. Locking control

The locking control unit consists of logic and PID controllers to select the control signal. Initially, a triangular signal is delivered to the piezoelectric actuator before locking. Once the lock point is selected through the GUI, the control unit outputs a PID-controlled signal to the actuator. The PID parameters, which include K_p, K_v, and K_a, can be adjusted to achieve efficient control. For our setup, the optimal values of K_p, K_v, and K_a are 715, 15, and 1 a.u, respectively.

3.5. Amplifier

The Red Pitaya's output voltages are insufficient for driving the piezo and obtaining a proper laser spectrum. To address this, an external non-inverting amplifier circuit using an OP27 with an 8 MHz bandwidth is employed to amplify the control signal with a gain of 11. The circuit diagram for the amplifier is shown in Fig. 2(b). The gain of the amplifier can be calculated as:

$$A_v = 1 + \frac{R_f}{R_1} \tag{1}$$

Here A_v is the gain of the amplifier. $R_f = 10$ kΩ, $R_1 = 1$ kΩ are the feedback and input resistor values.

$$V_{Amp} = A_v V_{control} sin(2\pi f_m t) + V_n sin(2\pi f_n t) \tag{2}$$

Here V_{Amp} is the amplified triangular or scan signal. $V_{control} sin(2\pi f_m t)$ is the controlled signal for scanning the laser, $V_{control}$ is the amplitude of controlled signal, f_m is the frequency of the controlled signal, V_n is the noise signal amplitude, f_n is the noise signal frequency $(f_n \gg f_m)$.

3.6. DC offset adder

The tunable DC offset signal added to the amplified signal can be used to fine-tune the laser spectrum and drive the piezo actuator with positive voltage. This DC offset signal is obtained using a DC adder circuit designed using an LTC6090 operational amplifier with a bandwidth of 12 MHz and four 1 kΩ resistors, as shown in Fig. 2(b). The circuit provides unity gain amplification to the signal.

The resulting signal can be expressed as:

$$V_{Adder} = V_{offset} + A_v V_{control} sin(2\pi f_m t) + V_n sin(2\pi f_n t) \tag{3}$$

Here, V_{Adder} is the tunable DC signal along with the amplified signal, V_{offset} is the DC offset voltage, A_v is the gain of the amplifier, $V_{control}$ is the controlled scan signal.

A variable DC voltage in the 0 to 15 V range is obtained using a potentiometer (POT) in the system, as shown in the OP27 buffer block in Fig. 2(b). The offset adder can also be used for fine-tuning the grating, as it was found that the frequency can be tuned up to 350 MHz without adjusting any other components.

3.7. Filter

To improve the system's performance, a low-pass filter is employed to remove high-frequency noise from the DC-coupled amplified signal, which affects the system's operation in the 0 to 10 Hz frequency range [15]. This filter not only sharpens the scan signal but also minimizes the errors in laser locking. A second-order Sallen-Key low-pass filter topology [16] is used, with a cut-off frequency of 795 ± 5 Hz. The cut-off frequency, which is determined by resistor and capacitor values, is given by the following equation:

$$f_c = \frac{1}{\sqrt{2\pi R_8 R_9 C_1 C_2}} \tag{4}$$

where f_c is the cut-off frequency, R_8 and R_9 are resistor values of 2 MΩ, and C_1 and C_2 are capacitor values of 100 pF each. After filtering, the resulting voltage is the same as that of the DC voltage adder, and is expressed as:

$$V_{Filter} = V_{offset} + A_v V_{control} sin(2\pi f_m t) \tag{5}$$

where V_{Filter} is the filtered signal, A_v is the amplifier gain, and $V_{control}$ is the controlled scan signal. The frequency order is $f_n > f_c > f_m$.

3.8. Buffer

In the designed circuit, two buffer circuits are incorporated to prevent the loading effect between the POT and the DC offset adder and between the filter and the load compensator. These buffer circuits ensure that the input signal is transmitted to the output without any distortion or loss, as depicted in Fig. 2(b).
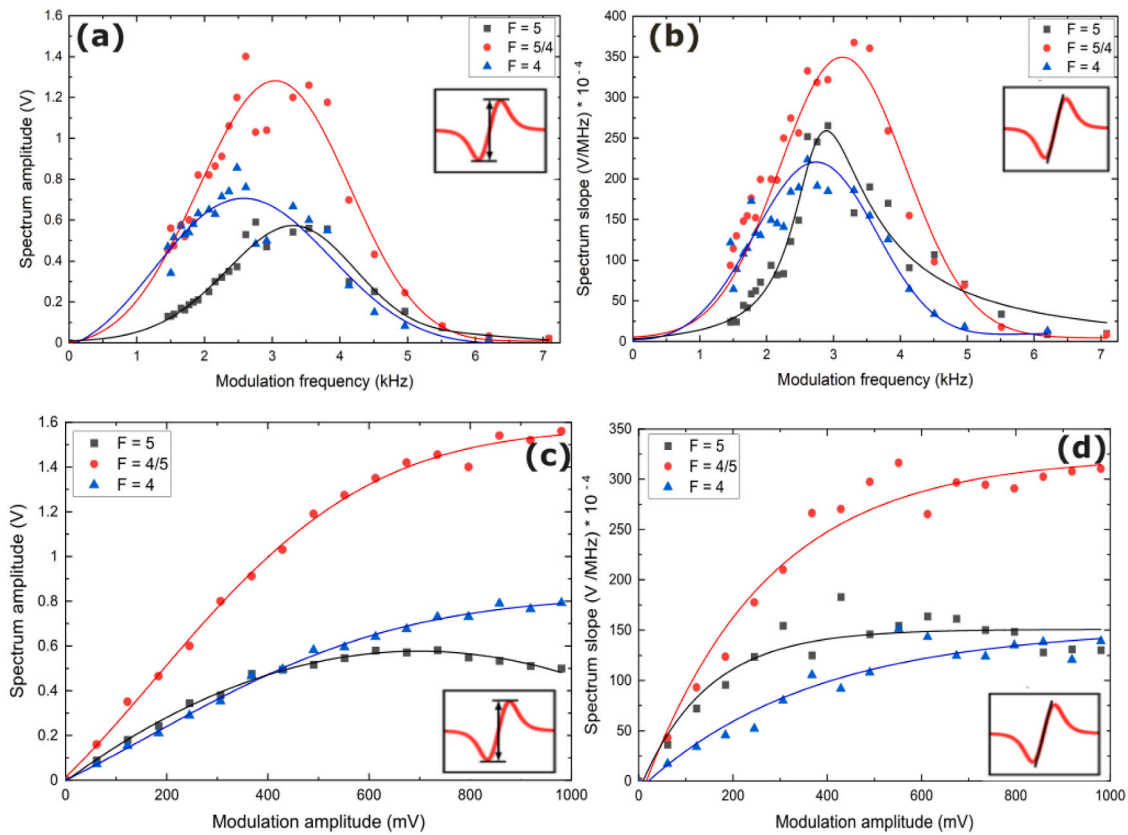
Fig. 4. Figure (a) and (b) show the amplitude and slope of the FM spectrum, respectively, as a function of the modulation frequency while keeping the modulation amplitude constant at $f_{amp.} = 306.4$ mV. Similarly, figures (c) and (d) display the effect of changing the modulation amplitude at a fixed modulation frequency of $f_{freq.} = 3.82 \pm 0.04$ kHz.

3.9. Load compensator

The DC-coupled amplified signal drives the piezo-actuator, which acts as a capacitive load. However, large capacitive loads can have a detrimental effect on system stability. In this design, the load capacitance is within the range of 345 nF, which is relatively high but still stable. A POT with a low resistance value is introduced to address this issue. The tunability of the POT enables the system to accommodate various piezo loads. The load compensating POT is highlighted in green in Fig. 2(b).

3.10. Piezo-actuator

Piezoelectric actuators are precision ceramic actuators that convert electrical energy directly into linear motion with high speed and force. A piezoelectric actuator adjusts the mirror position according to the applied voltage in this system. The output voltage of the electronic box, which serves as the input voltage to the piezoelectric actuator, is given by:

$$V_{out} = V_{offset} + A_v V_{control} \sin(2\pi f_m t) \tag{6}$$

The characteristics of the electronic box when $V_{offset} = 0$ are shown in Fig. 2(c). The input voltage varies from 0 to 2 V and is measured as the output voltage. The characteristic curve exhibits a linear nature and matches the theoretical analysis. Similarly, the electronic box input frequency is changed from 0 to 10 Hz, and the output voltage is measured. As the output voltage is frequency-independent, there is no effect on the output voltage due to changes in input frequency.

3.11. Graphical user interface

A GUI has been customized to enable control of the experimental setup (as illustrated in Fig. 1) and analysis of output signals. The GUI communicates with the FPGA and allows for the adjustment of parameters for the scope, triangular signal generator, PID controller, modulator, demodulator, and filter. Each module's parameters can be continuously tuned to achieve the desired output. For example, the scan signal's amplitude maximum, amplitude minimum, and frequency parameters are adjustable. In the case of the PIDs, the parameters K_p, K_v, and K_a can be adjusted. In the case of the modulator, modulation amplitude and frequency parameters are tunable, while in the case of the demodulator, the cut-off frequency can be adjusted. The GUI also provides the option to route necessary input and output signals to the system module. Overall, the designed GUI interface simplifies the process of laser locking and makes it user-friendly.

4. Frequency modulation spectroscopy

Frequency Modulation Spectroscopy (FMS) is a highly precise and sensitive method of spectroscopy that was first introduced by Bjorklund in the 1980s [17,18]. The traditional technique of FMS involves carrier frequency and sideband frequencies, with the modulation frequency acting as a sideband frequency. In this method, a carrier beam, combined with the modulation frequency, passes through an atomic medium, and the resulting output is detected by a photodetector (PD) and demodulated using various electronic components [19].

The detected spectrum in FMS is a complex combination of absorption and dispersion signals [18,20], along with the spectroscopic properties observed in the detected probe. FMS modulation can be achieved through the optical carrier's external or internal modulation, with electro-optic phase modulators being used in both methods [19–21]. It can also be achieved by directly modulating the current injected into a laser diode [22].

In FMS, the modulated electromagnetic field interacts with the atomic medium within the thermal cell, and the detected intensity profile reveals the characteristics of the resonance.

Table 1

Summary provides information on the maximum signal amplitude and slope of the observed zero crossing for each transition.

Atomic transition	Modulation frequency		Modulation amplitude		I_{Probe}/I_{Sat}		I_{Pump}/I_{Sat}	
	Ampl. (V)	Slope (V/MHz) $\times 10^{-4}$	Ampl. (V)	Slope (V/MHz) $\times 10^{-4}$	Ampl. (V)	Slope (V/MHz) $\times 10^{-4}$	Ampl. (V)	Slope (V/MHz) $\times 10^{-4}$
F = 4 → F′ = 5	0.59 ± 0.03	266.1 ± 0.06	0.58 ± 0.04	184.0 ± 0.06	0.80 ± 0.02	287.01 ± 0.03	0.57 ± 0.01	235.9 ± 0.02
F = 4 → F′ = 5/4	1.42 ± 0.02	368.15 ± 0.07	1.56 ± 0.06	316.2 ± 0.1	1.43 ± 0.01	320.18 ± 0.08	1.45 ± 0.05	468.42 ± 0.04
F = 4 → F′ = 4	0.85 ± 0.04	223.81 ± 0.03	0.82 ± 0.01	140.17 ± 0.01	0.72 ± 0.07	168.67 ± 0.02	0.84 ± 0.02	338.52 ± 0.05

Fig. 1 shows the design schematic of the FPGA-based programmable chip feedback system used in FMS. This system directly modulates the injection voltage to control the ECDL laser, with the FPGA controlling the laser by manipulating the position of the frequency-selective grating inside it. The saturation absorption spectrum modulated with a sinusoidal wave of specific frequency and amplitude is detected by the PD inside the locking box. The modulated signal can subsequently be amplified and processed using a higher-order low-pass filter for better resolution. The parameters mentioned above can be tuned using the GUI, which enables systematic optimization of the zero-crossing atomic signal.

The feedback system generates a zero crossing signal that reflects the difference between the set point and the fundamental laser frequency. The PID regulator works to minimize this difference by considering the error signal's present, past, and possible future values through proportional, integral, and derivative terms, respectively. By taking the derivative of the spectroscopic spectrum, a sharp and linear zero crossing can be obtained at an atomic resonance position, which serves as the desired error signal.

To achieve this derivative, Heterodyne Spectroscopy (HDS) is used by modulating the laser frequency with ω_m, which can be considered as sidebands with $\pm\omega_m$. The laser beam passes through the thermal cell, and the beam's intensity (I) is detected using a photo-diode. When the trim modulation amplitude M_m is sufficiently small, the measured beam intensity can be expressed as:

$$I(t) = I_0[1 + M_m\delta\cos(\omega_m t) + M_m\phi\sin(\omega_m t)] \tag{7}$$

This equation describes the measured intensity of the laser beam after passing through a thermal cell in the presence of modulation. The unmodulated beam intensity is denoted by I_0, and the parameters δ and ϕ are related to the loss difference encountered by the two sidebands and the phase shift difference between the laser frequency and the sidebands, respectively. The frequency of modulation denoted as ω_m, is significantly smaller compared to the spectral width. The values of δ and ϕ are directly proportional to the first and second derivatives of dispersion, respectively. Demodulation of the signal is achieved by multiplying it with a sinusoidal wave having a frequency of ω_m and a phase of θ. The intensity measured is expressed as follows:

$$I(t)\cos(\omega_m t + \theta) = I_0 M_m/2[\delta\cos(\theta) - \phi\sin(\theta) + \\ 2/M_m\cos(\omega_m t + \theta) + \theta\cos(2\omega_m t + \theta) + \\ \theta\sin(2\omega_m t + \theta)] \tag{8}$$

The overall spectrum contains three primary parameters that depend on ω_m. However, these parameters are typically eliminated by a low-pass filter in regular practice. By setting θ to zero, the parameter ϕ can be removed, and the derivative δ can be obtained and used for feedback.

4.1. Frequency modulation

Our system receives input signals from a saturated absorption spectroscopy setup to stabilize the laser. A diagram of the information flow inside the FPGA can be found in Fig. 1, with more details to follow in the subsequent sections. The laser emits a beam of 852.35 nm wavelength that passes through a Cs vapor cell containing the ^{133}Cs isotope. The saturated absorption spectrum is detected using a PD, as shown in Fig. 2(d). We calibrated the frequency axis using the separation between the F = 4 → F′ = 5 and F = 4 → F′ = 4 transitions, which we measured to be 251 MHz. The spectrum exhibits four prominent zero-crossing FM peaks: F = 4 → F′ = 5, F = 4 → F′ = 5/4 (crossover), F = 4 → F′ = 4, and F = 4 → F′ = 3/4 (crossover), as shown in Fig. 2 (d).

Our laser is locked to the crossover peak between the F = 4 → F′ = 5 and F = 4 → F′ = 4 transitions of the ^{133}Cs-D2 line for our experiments. However, it is possible to efficiently lock any of the four zero crossings depending on the experimental requirements. We use a modified GUI application, based on previous works [23,24], to control the entire laser locking process and display relevant data on the computer interface, as shown in Fig. 1. The modulation of the spectrum is accomplished using a sinusoidal wave generated by an FPGA-based digital function generator, which is subsequently demodulated by a built-in digital low-pass filter with a cut-off frequency of 307.1 kHz to eliminate high-frequency modulated signals. The modulation frequency, amplitude, and signal slope are systematically adjusted to obtain appropriate design parameters. The modulation frequency that yields the peak amplitude and slope is approximately 3.7 ± 0.4 kHz, 3.2 ± 0.4 kHz, and 2.5 ± 0.4 kHz for F = 4 → F′ = 5, F = 4 → F′ = 5/4, and F = 4 → F′ = 4, respectively, as shown in Fig. 4(a) and (b). Table 1 summarizes the maximum amplitude and slope achieved during the experiments. A lower modulation frequency is not desirable as it limits the bandwidth of the locking circuit, while a smaller modulation amplitude results in lower absorption disparity encountered by the sidebands. Technical constraints, such as the FPGA speed, determine the system's bandwidth at high frequencies.

4.2. Amplitude modulation

We conducted experiments to determine the optimal amplitude of the modulated signal, which we varied for three transitions: F = 4 → F′ = 5, F = 4 → F′ = 5/4 (crossover), and F = 4 → F′ = 4. We found that after reaching approximately 700 ± 50 mV, the amplitude and slope remained almost constant, as shown in Fig. 4(d). We summarized the maximum slope and amplitude during our experiments in Table 1. For each transition, the behavior was initially exponential until around 550 ± 50 mV, after which it approached saturation. The corresponding data is presented in Fig. 4(c) and (d). Therefore, we determined that the optimized amplitude and slope is around 600 ± 50 mV, which we used for the rest of the experiments. We fed the optimized zero crossing signal into the in-built PID controller, which generated a feedback signal to maintain the lock in a closed-loop fashion.

5. Beam intensity calibration

In this section, we discuss the optimization of beam intensity and the characterization of the locking technique, with a focus on three transitions: F = 4 → F′ = 5, F = 4 → F′ = 5/4 (crossover), and F = 4 → F′ = 4. The primary goal of laser locking is to achieve fast recovery from disturbances, which depends on the steepness of the zero-crossing spectrum slope that is modulated by the amplitude. Additionally, the amplitude is critical for improving the signal-to-noise ratio. However, the linewidth increases at considerably higher modulation amplitudes. Therefore, the modulation amplitude should be adjusted based on the beam's purpose. To optimize and characterize the locking technique,
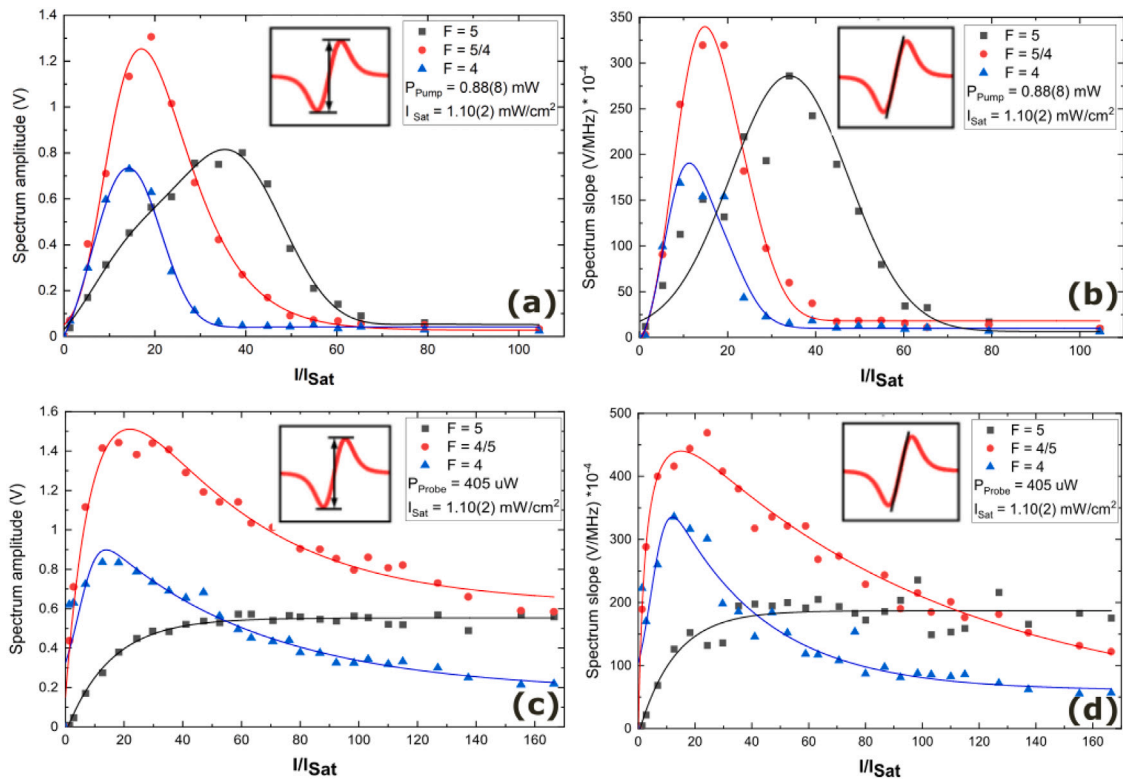
Fig. 5. The figure shows the relationship between the amplitude and slope of the FM spectrum versus pump and probe intensity, which are normalized by the saturation intensity of the D2 transition of Cs. Panels (a) and (b) depict the variation of probe intensity while keeping the pump power constant at 0.88 ± 0.08 mW, while panels (c) and (d) show the variation of pump power while keeping the probe power constant at 405 μW. The data is normalized by the saturation intensity of the D2 transition of Cs, which is measured to be 1.10 ± 0.02 mW/cm^2.

we measure the system response as a function of the pump and probe intensities.

To maximize the slope of the FMS spectrum, we conducted experiments over a range of modulation amplitudes with a fixed modulation frequency of 3.82 ± 0.04 kHz, as shown in Fig. 5. Each experiment was repeated five times, and the slope was determined using a linear fit. All data points were normalized by the saturated intensity of the D2 transition (i.e., $I_{Sat} = 1.10 \pm 0.02$ mW/cm^2), and the pump and probe beam dimensions were $\omega_x = 0.91 \pm 0.2$ mm, $\omega_y = 1.2 \pm 0.4$ mm and $\omega_x = 0.93 \pm 0.07$ mm, $\omega_y = 1.20 \pm 0.06$ mm, respectively. Initially, we varied the probe power while keeping the pump power constant at $P_{pump} = 0.88 \pm 0.8$ mW, and measured the peak-to-peak amplitude in Fig. 5(a) and the slope in Fig. 5(b) of the spectrum for three individual transitions.

We found that the amplitude and slope increased rapidly and then decreased sharply as we increased the probe power. For the $F = 4 \rightarrow F' = 5$ transition, the amplitude and slope peaked at $\sim 40 I/I_{Sat}$, represented by black square data points. For the $F = 4 \rightarrow F' = 5/4$ crossover transition, the maximum value was obtained at $\sim 20 I/I_{Sat}$, indicated by red circle data points. Similarly, for the $F = 4 \rightarrow F' = 4$ transition, the peak occurred around $\sim 18 I/I_{Sat}$, represented by blue triangular data points.

In addition, we performed experiments where we kept the probe power fixed at $P_{pump} = 0.40 \pm 0.05$ mW and varied the pump power amplitude. The results are shown in Fig. 5(c) and (d). For the $F = 4 \rightarrow F' = 5$ transitions, we observed that the amplitude and slope initially increased and then saturated at $\sim 30 I/I_{Sat}$, as denoted by black square data points. For the $F = 4 \rightarrow F' = 5/4$ crossover transition, the maximum value was obtained at $\sim 20 I/I_{Sat}$, as denoted by red circle data points. Similarly, for the $F = 4 \rightarrow F' = 4$ transition, the amplitude peaked at $\sim 18 I/I_{Sat}$, as denoted by blue triangular data points. We fitted the data points with an exponential function to identify the maximum amplitude and slope and summarized the results for each transition in Table 1.

Gaussian profiles were used to fit all the data points in Fig. 5(a) and (b) to determine their nature.

6. Locking to cesium atomic transitions

To assess the stability of our system using FM spectroscopy, we locked the laser onto an FMS peak corresponding to the $F = 4 \rightarrow F' = 5/4$ (crossover) transition of the D2 line of Cs. We then took long-term frequency fluctuation measurements, as shown in Fig. 6, and estimated the power spectral density (PSD) of the free-running and locked laser, as shown in Fig. 6(b). The laser output was monitored at a 10 ms repetition rate using a wavelength meter (highfinesse, WS-08-2).

To determine the frequency fluctuations of the laser before and after locking, we sent the light from one laser to a photodetector and recorded the signal using a signal analyzer. We observed that the frequency fluctuations were significantly reduced after locking. After measuring the long-term stability, we measured the frequency fluctuations using a wavelength meter (with an uncertainty of ± 2 MHz) and found that the frequency fluctuation of the laser was less than 4 MHz (peak-to-peak value) in Fig. 6(b), which is smaller than the natural linewidth of the D2 line of Cs, which is 5.234(13) MHz [25,26]. Fig. 6(c) also shows that the frequency fluctuations were significantly reduced after locking.

However, it is important to note that the limitations of the wavelength meter may make it impossible to measure frequency fluctuations less than 4 MHz. Therefore, we strongly believe that the actual value of the frequency fluctuations after laser locking must be less than 1 MHz.

7. Conclusion

In summary, we have successfully developed a low-cost and versatile laser frequency stabilization system using direct frequency modulation on an FPGA-based platform. The system has been validated
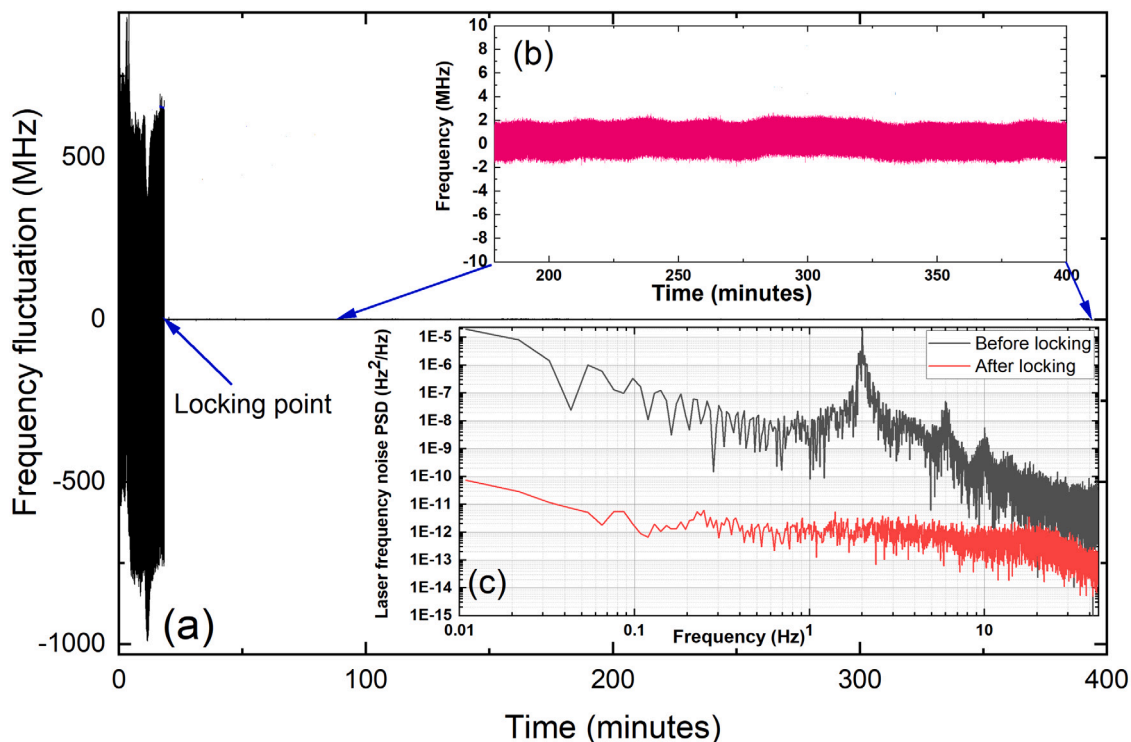
Fig. 6. Figure (a) illustrates the frequency fluctuation of the laser over a period of 6 h, both before and after laser locking. In Figure (b), the standard deviation of frequency fluctuation after locking is shown, estimated to be 0.64 ± 0.03 MHz. Figure (c) shows the power spectral density of the frequency fluctuations of the laser, with the unlocked state represented by the black line and the locked state represented by the red line.

Table 2
The table summarizes the total price estimation involved in the project. Each row represents a specific item or expense.

Price list		
Item	Remarks	Price in USD
Power supply	Local source	15
Red Pitaya	Ref. [27]	340
Chip - OP027	Local source	2
Chip - LT6090	Local source	25
Electric cable	Local source	2
3D Printed Casing	Home-built	5
Miscellaneous	Other components	10 (approx.)
Total		399

using three different methods and has demonstrated exceptional lock stability for more than 6 h, with a frequency standard deviation of less than 700 kHz at 852.35 nm. The system is easy to use and can be applied in various experimental setups, including signal and PSD measurements for spectroscopy optimization. Moreover, the production cost of a single unit is less than $500 as described in 2, making it an affordable alternative to conventional systems.

In future work, we plan to explore using different OP-AMPs to generate more scan ranges and incorporate other techniques like Modulation transfer spectroscopy [28,29] and offset locking scheme to enhance the stability further. We also suggest using the beat note technique [30] for accurately estimating the laser's linewidth. Furthermore, we recognize the importance of an ultra-stable power supply in achieving precise and consistent results. In recent research, molecules have been cooled directly using stable cavities, as demonstrated in studies such as [31–33]. The Pound–Drever–Hall technique has played a pivotal role in achieving this cooling process [34]. It's worth noting that our technique holds promise for potential applications in molecular

spectroscopy as demonstrated in the work conducted by researchers in the Ref. [35].

Declaration of competing interest

The authors declare the following financial interests/personal relationships which may be considered as potential competing interests: Prosenjit Majumder reports financial support, administrative support, equipment, drugs, or supplies, statistical analysis, and writing assistance were provided by Department of Physics, Indian Institute of Technology, Delhi, Hauz Khas, Delhi, 110016, New Delhi, India.

Data availability

Data will be made available on request.

Acknowledgments

References

[1] M.S. Safronova, D. Budker, D. DeMille, D.F.J. Kimball, A. Derevianko, C.W. Clark, Search for new physics with atoms and molecules, Rev. Modern Phys. 90 (2018) 025008, http://dx.doi.org/10.1103/RevModPhys.90.025008, URL https://link.aps.org/doi/10.1103/RevModPhys.90.025008.

[2] E. Burt, J. Prestage, R. Tjoelker, D. Enzer, D. Kuang, D. Murphy, D. Robison, J. Seubert, R. Wang, T. Ely, Demonstration of a trapped-ion atomic clock in space, Nature 595 (7865) (2021) 43–47, http://dx.doi.org/10.1038/s42254-021-00342-1.

[3] X. Wu, Z. Pagel, B.S. Malek, T.H. Nguyen, F. Zi, D.S. Scheirer, H. Müller, Gravity surveys using a mobile atom interferometer, Sci. Adv. 5 (9) (2019) eaax0800, http://dx.doi.org/10.1126/sciadv.aax0800, arXiv:https://www.science.org/doi/pdf/10.1126/sciadv.aax0800. URL https://www.science.org/doi/abs/10.1126/sciadv.aax0800.

[4] K. Bongs, M. Holynski, J. Vovrosh, P. Bouyer, G. Condon, E. Rasel, C. Schubert, W.P. Schleich, A. Roura, Taking atom interferometric quantum sensors from the laboratory to real-world applications, Nat. Rev. Phys. 1 (12) (2019) 731–739, http://dx.doi.org/10.1038/s42254-019-0117-4.

[5] A. Schwettmann, J. Sedlacek, J.P. Shaffer, Field-programmable gate array based locking circuit for external cavity diode laser frequency stabilization, Rev. Sci. Instrum. 82 (10) (2011) 103103, http://dx.doi.org/10.1063/1.3646477, arXiv:https://doi.org/10.1063/1.3646477.

[6] T. Preuschoff, M. Schlosser, G. Birkl, Digital laser frequency and intensity stabilization based on the STEMlab platform (originally Red Pitaya), Rev. Sci. Instrum. 91 (8) (2020) 083001, http://dx.doi.org/10.1063/5.0009524, arXiv:https://doi.org/10.1063/5.0009524.

[7] G.P. Conangla, F. Ricci, M.T. Cuairan, A.W. Schell, N. Meyer, R. Quidant, Optimal feedback cooling of a charged levitated nanoparticle with adaptive control, Phys. Rev. Lett. 122 (2019) 223602, http://dx.doi.org/10.1103/PhysRevLett.122.223602, URL https://link.aps.org/doi/10.1103/PhysRevLett.122.223602.

[8] I. Morgenstern, S. Zhong, Q. Zhang, L. Baker, J. Norris, B. Tran, A. Schwettmann, A versatile microwave source for cold atom experiments controlled by a field programmable gate array, Rev. Sci. Instrum. 91 (2) (2020) 023202, http://dx.doi.org/10.1063/1.5127880, arXiv:https://doi.org/10.1063/1.5127880.

[9] M. Koch, C. Sames, A. Kubanek, M. Apel, M. Balbach, A. Ourjoumtsev, P.W.H. Pinkse, G. Rempe, Feedback cooling of a single neutral atom, Phys. Rev. Lett. 105 (2010) 173003, http://dx.doi.org/10.1103/PhysRevLett.105.173003, URL https://link.aps.org/doi/10.1103/PhysRevLett.105.173003.

[10] D.A. Hopper, J.D. Lauigan, T.-Y. Huang, L.C. Bassett, Real-time charge initialization of diamond nitrogen-vacancy centers for enhanced spin readout, Phys. Rev. Appl. 13 (2020) 024016, http://dx.doi.org/10.1103/PhysRevApplied.13.024016, URL https://link.aps.org/doi/10.1103/PhysRevApplied.13.024016.

[11] A. Bahrami, M. Müller, M. Drechsler, J. Joger, R. Gerritsma, F. Schmidt-Kaler, Operation of a microfabricated planar ion-trap for studies of a Yb+–Rb hybrid quantum system, Phys. Status Solidi (b) 256 (9) (2019) 1800647, http://dx.doi.org/10.1002/pssb.201800647, arXiv:https://onlinelibrary.wiley.com/doi/pdf/10.1002/pssb.201800647. URL https://onlinelibrary.wiley.com/doi/abs/10.1002/pssb.201800647.

[12] I.D. Conway Lamb, J.I. Colless, J.M. Hornibrook, S.J. Pauka, S.J. Waddy, M.K. Frechtling, D.J. Reilly, An FPGA-based instrumentation platform for use at deep cryogenic temperatures, Rev. Sci. Instrum. 87 (1) (2016) 014701, http://dx.doi.org/10.1063/1.4939094, arXiv:https://doi.org/10.1063/1.4939094.

[13] G.A. Stimpson, M.S. Skilbeck, R.L. Patel, B.L. Green, G.W. Morley, An open-source high-frequency lock-in amplifier, Rev. Sci. Instrum. 90 (9) (2019) 094701, http://dx.doi.org/10.1063/1.5083797, arXiv:https://doi.org/10.1063/1.5083797.

[14] M.A. Luda, M. Drechsler, C.T. Schmiegelow, J. Codnia, Compact embedded device for lock-in measurements and experiment active control, Rev. Sci. Instrum. 90 (2) (2019) 023106.

[15] R. Tirupathi, S.K. Kar, Low-offset differential output switched-capacitor interface for micro-capacitive acceleration sensors, IET Sci. Meas. Technol. 15 (3) (2021) 279–291, http://dx.doi.org/10.1049/smt2.12029, URL https://ietresearch.onlinelibrary.wiley.com/doi/abs/10.1049/smt2.12029.

[16] R. Tirupathi, S.K. Kar, A 200 $\mu g/\sqrt{Hz}$, 2.7 milli-g offset differential interface for capacitive micro accelerometer, IEEE Trans. Circuits Syst. II 68 (6) (2021) 1753–1757, http://dx.doi.org/10.1109/TCSII.2020.3041614.

[17] G.C. Bjorklund, Frequency-modulation spectroscopy: a new method for measuring weak absorptions and dispersions, Opt. Lett. 5 (1) (1980) 15–17, http://dx.doi.org/10.1364/OL.5.000015, URL http://opg.optica.org/ol/abstract.cfm?URI=ol-5-1-15.

[18] G.C. Bjorklund, M. Levenson, W. Lenth, C. Ortiz, Frequency modulation (FM) spectroscopy, Appl. Phys. B 32 (3) (1983) 145–152, http://dx.doi.org/10.1007/BF00688820.

[19] F. Zi, X. Wu, W. Zhong, R.H. Parker, C. Yu, S. Budker, X. Lu, H. Müller, Laser frequency stabilization by combining modulation transfer and frequency modulation spectroscopy, Appl. Opt. 56 (10) (2017) 2649–2652, http://dx.doi.org/10.1364/AO.56.002649, URL https://opg.optica.org/ao/abstract.cfm?URI=ao-56-10-2649.

[20] I. Ben-Aroya, M. Kahanov, G. Eisenstein, Multi-field frequency modulation spectroscopy, Opt. Express 16 (9) (2008) 6081–6097, http://dx.doi.org/10.1364/OE.16.006081, URL http://opg.optica.org/oe/abstract.cfm?URI=oe-16-9-6081.

[21] Q.A. Duong, T.D. Nguyen, T.T. Vu, M. Higuchi, D. Wei, M. Aketagawa, Suppression of residual amplitude modulation appeared in commercial electro-optic modulator to improve iodine-frequency-stabilized laser diode using frequency modulation spectroscopy, J. Eur. Opt. Soc.-Rapid Publ. 14 (1) (2018) 1–12, http://dx.doi.org/10.1186/s41476-018-0092-x.

[22] T. Preuschoff, P. Baus, M. Schlosser, G. Birkl, Wideband current modulation of diode lasers for frequency stabilization, Rev. Sci. Instrum. 93 (6) (2022) 063002, http://dx.doi.org/10.1063/5.0093520, arXiv:https://doi.org/10.1063/5.0093520.

[23] M.A. Luda, M. Drechsler, C.T. Schmiegelow, J. Codnia, Compact embedded device for lock-in measurements and experiment active control, Rev. Sci. Instrum. 90 (2) (2019) 023106, http://dx.doi.org/10.1063/1.5080345, arXiv:https://doi.org/10.1063/1.5080345.

[24] B. Wiegand, B. Leykauf, R. Jördens, M. Krutzik, Linien: A versatile, user-friendly, open-source FPGA-based tool for frequency stabilization and spectroscopy parameter optimization, Rev. Sci. Instrum. 93 (6) (2022) 063001, http://dx.doi.org/10.1063/5.0090384, arXiv:https://doi.org/10.1063/5.0090384.

[25] D.A. Steck, Cesium D line data, 2003, URL https://steck.us/alkalidata/cesiumnumbers.pdf.

[26] T. Udem, J. Reichert, T.W. Hänsch, M. Kourogi, Absolute optical frequency measurement of the cesium D_2 line, Phys. Rev. A 62 (2000) 031801, http://dx.doi.org/10.1103/PhysRevA.62.031801, URL https://link.aps.org/doi/10.1103/PhysRevA.62.031801.

[27] Red pitaya, 2023, accessed on 05.24.2023. URL https://redpitaya.com/.

[28] H.-R. Noh, S.E. Park, L.Z. Li, J.-D. Park, C.-H. Cho, Modulation transfer spectroscopy for 87Rb atoms: theory and experiment, Opt. Express 19 (23) (2011) 23444–23452, http://dx.doi.org/10.1364/OE.19.023444, URL https://opg.optica.org/oe/abstract.cfm?URI=oe-19-23-23444.

[29] P. Majumder, Towards the Trapping of Single Potassium Atoms in Optical Tweezers (Ph.D. thesis), Durham University, 2022, URL https://discover.durham.ac.uk/permalink/44DUR_INST/1oe7agi/cdi_proquest_journals_2685131983.

[30] L. Hao, X. Wang, D. Guo, K. Jia, P. Fan, J. Guo, X. Ni, G. Zhao, Z. Xie, S. ning Zhu, Narrow-linewidth self-injection locked diode laser with a high-Q fiber Fabry–Perot resonator, Opt. Lett. 46 (6) (2021) 1397–1400, http://dx.doi.org/10.1364/OL.415859, URL https://opg.optica.org/ol/abstract.cfm?URI=ol-46-6-1397.

[31] E.S. Shuman, J.F. Barry, D.R. Glenn, D. DeMille, Radiative force from optical cycling on a diatomic molecule, Phys. Rev. Lett. 103 (2009) 223001, http://dx.doi.org/10.1103/PhysRevLett.103.223001, URL https://link.aps.org/doi/10.1103/PhysRevLett.103.223001.

[32] J.F. Barry, D.J. McCarron, E.B. Norrgard, M.H. Steinecker, D. DeMille, Magneto-optical trapping of a diatomic molecule, Nature 512 (7514) (2014) 286–289, http://dx.doi.org/10.1038/nature13634.

[33] B.K. Stuhl, B.C. Sawyer, D. Wang, J. Ye, Magneto-optical trap for polar molecules, Phys. Rev. Lett. 101 (2008) 243002, http://dx.doi.org/10.1103/PhysRevLett.101.243002, URL https://link.aps.org/doi/10.1103/PhysRevLett.101.243002.

[34] E.D. Black, An introduction to Pound–Drever–Hall laser frequency stabilization, Amer. J. Phys. 69 (1) (2001) 79–87, http://dx.doi.org/10.1119/1.1286663, arXiv:https://pubs.aip.org/aapt/ajp/article-pdf/69/1/79/10115998/79_1_online.pdf.

[35] L. Sharma, A. Roy, S. Panja, S. De, Stabilizing frequency of a diode laser to a reference transition of molecular iodine through modulation transfer spectroscopy, Atoms 11 (5) (2023) http://dx.doi.org/10.3390/atoms11050083, URL https://www.mdpi.com/2218-2004/11/5/83.